

Final Draft
of the original manuscript:

Bargmann, S.; Scheider, I.; Xiao, T.; Yilmaz, E.; Schneider, G.A.; Huber, N.:
Towards bio-inspired engineering materials: Modeling and simulation of the mechanical behavior of hierarchical bovine dental structure
In: Computational Materials Science (2013) Elsevier

DOI: [10.1016/j.commatsci.2013.06.028](https://doi.org/10.1016/j.commatsci.2013.06.028)

Towards bio-inspired engineering materials: Modeling and simulation of the mechanical behavior of hierarchical bovine dental structure

Swantje Bargmann^{a,b}, Ingo Scheider^a, Tao Xiao^a, Ezgi Yilmaz^c, Gerold A. Schneider^c, Norbert Huber^a

^a*Helmholtz-Zentrum Geesthacht, Institute of Materials Research, Geesthacht, Germany*

^b*Institute of Continuum Mechanics and Material Mechanics, Hamburg University of Technology, Germany*

^c*Institute of Advanced Ceramics, Hamburg University of Technology, Germany*

Abstract

Dental enamel is the outermost layer of a tooth crown consisting of a hierarchical and graded structure. Approx. 85 vol.% of enamel consist of the hydroxyapatite mineral, the rest being protein and water. This contribution is concerned with the modeling and computation of the mechanical behavior, in particular with the failure, of the enamel of a bovine tooth. For the underlying model description, we resort to a non-linear Neo-Hookean model for the mineral and to the Arruda-Boyce model for the protein, in combination with a cohesive zone approach. The model accounts for non-linear, large-deformation kinematics and softening at the first level hierarchy and it is validated against experimental data. The numerical implementation is carried out with the help of the finite element method. Here, we resort to a three-dimensional cohesive zone model which maps cracking of the mineral fibers as well as debonding between the mineral fiber and the protein. A complex microstructure representing bovine enamel is studied in the numerical examples. The results capture major features of the physical experiments, such as nonlinear stress-strain behavior, stiffness and failure strength.

Keywords: bovine teeth, dental enamel, cohesive zone model, size effect, fracture behavior

1. Introduction

Motivated by the fascinating mechanical properties of mineralized biological hierarchical materials, such as bone, dentine enamel or wood [1, 2, 3], research on the synthesis of biomimetic hierarchical organic/inorganic materials has been going on worldwide since about two decades. Most techniques are based on self-assembly [4, 5, 6, 7] and are restricted to only one level of hierarchy. Among the different methods, freeze casting allows producing materials very similar to nacre with distinguished fracture toughness [8, 9]. However, for freeze casting the first level of hierarchy is limited in the order of $1 - 10 \mu\text{m}$.

The Collaborative Research Center SFB 986 "Tailor-Made Multi Scale Materials Systems - M³", which has been established in Hamburg recently, aims at the synthesis of a self-similar hierarchical material with the first level of hierarchy well below $1 \mu\text{m}$ and a second level of hierarchy in the range of $1 - 10 \mu\text{m}$. First

results on the assembly of the first level of hierarchy have been published recently [10]. By adding another level of hierarchy, the question of the optimal design with respect to geometry and mechanical properties arises. The additional degrees of freedom result in a rather low chance of producing a material with improved properties based on an empirical approach alone.

To overcome this problem, it is important to understand and correctly predict the mechanisms of deformation and fracture of a material having more than one level of hierarchy. It is therefore crucial to start identifying the relevant properties and geometrical features of an existing hierarchical material on each level of hierarchy. This approach provides the required insight into the function of soft and hard phases as well as the interfaces in between and, furthermore, delivers a validated modeling approach. In the following, dental enamel is used as an optimized hierarchical material. A model is built for the first level of hierarchy based on the behavior of the real material, representing the fundamental building block for the next level.

Dental enamel is a load-bearing natural biocomposite, which has evolved to resist fracture and wear. The most striking behavior of enamel from the material scientist point of view is its longevity in the existence of cracks (under mastication stresses up to 2.5 GPa) in spite of its high mineral volume content. The mechanisms hindering the brittleness of this highly mineralized tissue have been mostly attributed to its hierarchical structuring and also its nanocomposite nature consisting of soft organic matter. For instance, the investigations on the structure-mechanical property relation of enamel could aid to develop human body armor [11], or aid for a better selection of dental restoratives [12].

In this work, we formulate a mathematical thermodynamically consistent model for the material behavior of dental enamel of bovine teeth which accounts for: i) size effects, ii) non-linear elasticity, and iii) softening and iv) different fracture mechanism. In this work, the mechanical behavior of the representative volume element (RVE)¹ is simulated representing the microstructure of the first hierarchy level based on Scheider et al. [15, 16].

The three-dimensional cohesive zone approach accounts for two failure modes: breaking of the mineral fiber and debonding of the interface between the mineral and the protein. We validate our model against experimental data. The model correctly predicts a size-dependent stress-strain response and different failure modes.

¹In general, the existence of an RVE is questionable as soon as localized material degradation and damage occurs, see e.g. [13, 14] - if the damage behavior is incorporated into the continuum model. In a cohesive model, damage and deformation are modeled by two different models, a continuum model and a cohesive model. Since the fracture process zone for the cohesive model is reduced to zero, the absolute size of it is incorporated in the model parameters and not in the geometry. The continuum model then only contains deformation.

2. Dental enamel of bovine teeth

Dental enamel, the hard protective layer of tooth crown, is a naturally occurring but a non-vital biological tissue. It has to survive millions of chewing cycles under complex-stress state conditions in the oral environment of the host even in the existence of severe internal cracks and flaws [17, 18]. In order to meet this functional requirements enamel should possess damage tolerance capability as evidenced in the recent studies [19, 20, 21, 22, 23, 24], which has been mainly attributed to the complex hierarchical and graded arrangement of its fiber-like mineral crystals and organic constituents.

The hierarchical organization of bovine enamel, which is very similar to human enamel, can be characterized in 3 different levels, see Fig. 1. The simplest and smallest structural units are hydroxyapatite (HAP) nano-fibers glued by proteins (level 1). At the next level of hierarchy HAP nano-fibers are grouped together to form micron-scale structures known as “enamel rods” (level 2) with a diameter of about $5\ \mu\text{m}$. These rods are covered by organic layers [25]. The rods arrange in a straight and parallel fashion in the layer close to the outer surface (outer enamel); however, in the inner layer close to the dentin (inner enamel), groups of rods with same orientation decussate each other periodically forming so-called “Hunter–Schreger bands” (level 3). The width of the bands vary between $20 - 50\ \mu\text{m}$ in bovine enamel. The mechanical properties such as the stress-strain behavior or the elastic modulus (see, e.g., [23]) differ greatly on the different hierarchical levels.

The mechanical functionality of enamels hierarchical structure is an on-going issue. For example, measurements with Vickers indents (Indentation Crack Lengths Method, [26]) gave a small fracture toughness of the order of $1\ \text{MPa m}^{1/2}$ [27, 28, 29]. This led to the prevailing opinion that enamel is a brittle material. More recently, R-curve measurements [20, 22] revealed that the fracture resistance of enamel rises up to $4\ \text{MPa m}^{1/2}$ due to its graded structure and toughening mechanisms operating on all hierarchical levels [19]. This offers an additional explanation for the well-known crack arrest at the dentin enamel junction [30]. In addition to a drop in the stress intensity factor for a crack crossing the dentin enamel junction due to an elastic modulus drop of a factor three, the toughness of long cracks in enamel is equal or may even surpass the toughness in dentin [22]. A quantitative mechanical understanding of these effects is only possible, if the complex hierarchical microstructure of enamel is modeled. First steps in this regard are Gao’s self-similar concepts [31]. In this paper, we intend to be closer to the real microstructure of enamel, which necessitates a numerical simulation based on the microstructure.

A non-linear elastic fracture mechanics model of an entire tooth is presented in Ichim et al. [32] who numerically study damage and fracture in enamel. However, their numerical results support that dentine possesses a higher fracture toughness than enamel. This is in contrast to our experimental results which show that the enamel’s fracture toughness is as large as dentine’s [21]. Crack propagation in human teeth

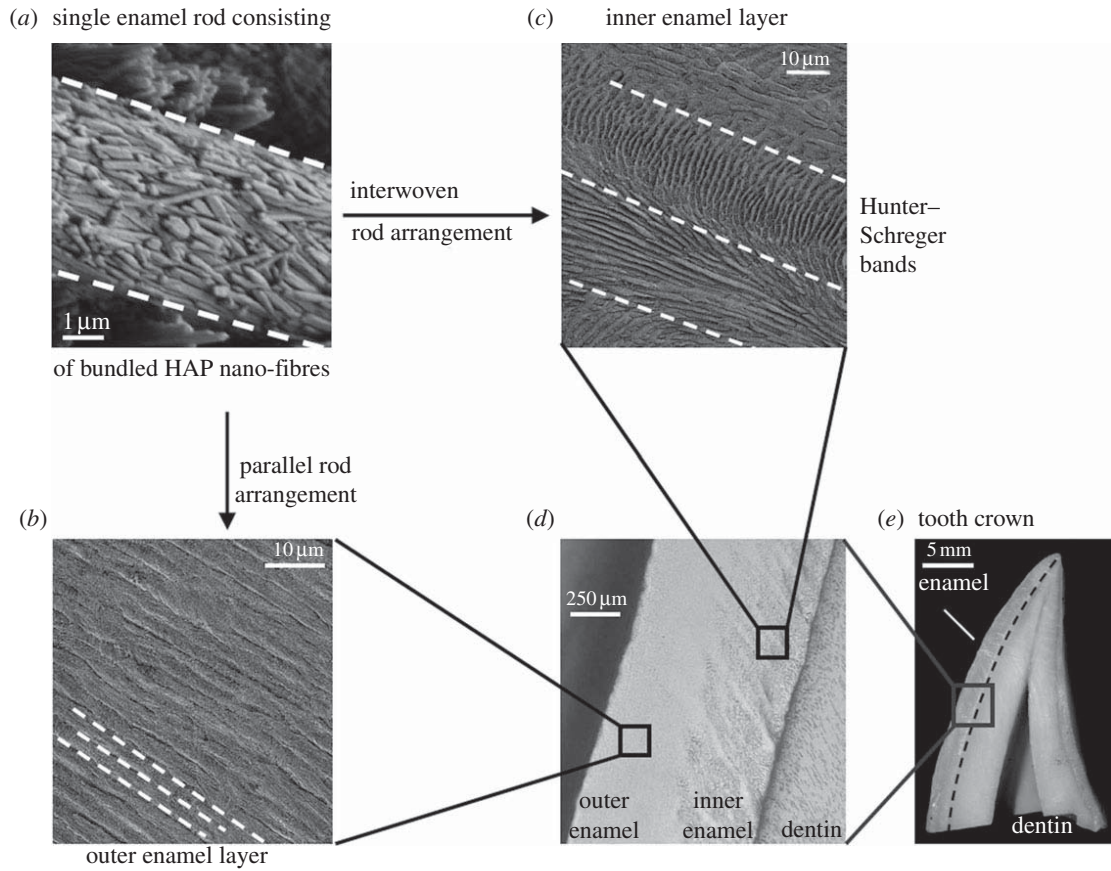


Figure 1: Hierarchical structure of bovine enamel. Picture taken from Bechtle et al. [23]. a) Single enamel rod consisting of bundled HAP nano-fibers (level 1: intra-rod). b) Outer enamel layer with parallel rod arrangement (level 2: multiple rods). c) Inner enamel layer with interwoven rod arrangement (level 3: Hunter-Schreger bands). d) Enlarged figure of the outer and inner enamel layer. e) Bovine teeth cross section.

based on the extended finite element method is computationally modeled in [33]. Both analyses are limited to the macroscale and completely ignore the underlying microstructure. A numerical study on the role of crystal arrangement and property gradients on the mechanical performance of enamel is presented by An et al. [34, 35]. Gao [31] discusses analytical solutions in a simple fracture mechanics concept. He applies it to hierarchical bones, but in general it is also applicable to hierarchical teeth. Yao and Gao [36] introduce a multi-scale cohesive law for self-similar hierarchical bone-like structures and present exact traction-separation curves for a premature model which allows for a first idea on the mechanics and mechanical properties of hierarchical materials. Wu et al. [37] present a constitutive theory for protein-based materials based on the Arruda-Boyce [38] model. The experimental findings on micropillars of hydroxyapatite-based exoskeleton of a fish of Han et al. [39] show that the direction dependence is less pronounced than expected by the orientation of the HAP fibers. In addition to the experiments, a finite element analysis on the micropillars

is presented. Their model is able to capture the anisotropic behavior of the ganoine under the compression deformation.

3. Continuum mechanical model

All physical processes are governed by the balance equations characterizing the state of any body. In the following, we concentrate on the mechanical behavior and, therefore, on the balance of momentum. We formulate all equations thermodynamically consistent and in a geometrically non-linear framework.

The linear balance of momentum expresses that the change of the total momentum $\rho\dot{\mathbf{u}}$ equals the sum over all forces acting on the body, i.e. the sum of the surface (contact) forces \mathbf{T} and the volume (far field) forces \mathbf{b} . The well-known Cauchy stress theorem relates the surface forces \mathbf{T} to a stress tensor, i.e., the first Piola–Kirchhoff stress tensor \mathbf{P} : via $\mathbf{T} = \mathbf{P} \cdot \mathbf{n}$. Application of the divergence theorem leads to

$$\rho\ddot{\mathbf{u}} = \text{Div}\mathbf{P} + \rho\mathbf{b}, \quad (1)$$

where $\mathbf{u} = \mathbf{x} - \mathbf{X}$ represents the linearized displacement. ρ denotes the constant material’s density. The first Piola–Kirchhoff stress tensor \mathbf{P} relates spatial forces to material area elements. It is related to the well-known Cauchy stress tensor $\boldsymbol{\sigma}$ via a push forward to the spatial configuration

$$\mathbf{P} = J\boldsymbol{\sigma} \cdot \mathbf{F}^{-t}, \quad (2)$$

with the Jacobian $J = \det\mathbf{F}$ and the deformation gradient \mathbf{F} .

The balance equation (1) is material-independent. Therefore, constitutive equations are introduced in order to describe the mechanical behavior of the tooth. In case of geometrically non-linear hyperelasticity, we assume that the constitutive equations to depend on the deformation gradient \mathbf{F} and that the free energy density ψ acts as a potential for the Cauchy stress:

$$\mathbf{P} = \frac{\partial\rho\psi}{\partial\mathbf{F}}. \quad (3)$$

The mineral and the protein phases have different material responses. In particular, the protein layer responses softer in comparison to the mineral fibers, cf. e.g. [23]. The material behavior of the mineral is modeled by the hyperelastic, non-linear Neo–Hookean law

$$\rho\psi_{\text{m}} = \frac{\mu_0}{2} \left[J^{-2/3} \text{tr}\mathbf{b} - 3 \right] + \frac{K}{2} [J - 1]^2, \quad (4)$$

with K being the initial bulk modulus, μ_0 is the initial shear modulus, and $\mathbf{b} := \mathbf{F} \cdot \mathbf{F}^t$ is the left Cauchy–Green strain tensor. Thus, the first Piola–Kirchhoff stress tensor reads

$$\mathbf{P}_{\text{m}} = \mu_0 J^{-2/3} \left[-\mathbf{F}^{-t} - \frac{1}{3} \text{tr}\mathbf{b} \mathbf{F}^{-t} \right] + K [J - 1] J \mathbf{F}^{-t}. \quad (5)$$

For the protein, following [37], we resort to the hyperelastic model based on Arruda–Boyce [38] to describe the non-linear elastic mechanical behavior of the dental enamel, i.e.,

$$\rho\psi_p := \mu \sum_{j=1}^5 \frac{C_j}{\lambda^{2j-2}} \left[(J^{-2/3} \text{tr} \mathbf{b})^j - 3^j \right] + \frac{K}{2} \left[\frac{J^2 - 1}{2} - \ln J \right], \quad (6)$$

where

$$C_1 = \frac{1}{2}, \quad C_2 = \frac{1}{20}, \quad C_3 = \frac{11}{1050}, \quad C_4 = \frac{19}{7000}, \quad C_5 = \frac{519}{673750}.^2 \quad (7)$$

$\mu_0 = \mu \left[1 + \frac{3}{5\lambda^2} + \frac{99}{175\lambda^4} + \frac{513}{875\lambda^6} + \frac{42039}{67375\lambda^8} \right]$ relates the initial shear modulus to μ , and λ is referred to as the locking stretch. Consequently, we obtain

$$\mathbf{P}_p = 2\mu \sum_{j=1}^5 \frac{j J^{-\frac{2}{3}j} C_j}{\lambda^{2j-2}} \left[[-\mathbf{F}^{-t}]^{j-1} - \frac{1}{3} \mathbf{F}^{-t} (\text{tr} \mathbf{b})^j \right] + \frac{K}{2} [J^2 - 1] \mathbf{F}^{-t}. \quad (8)$$

Inserting the constitutive equation into the balance equation (1) leads to

$$\rho \ddot{\mathbf{u}} = \begin{cases} \text{Div} \left(\mu_0 J^{-2/3} [\mathbf{F}^{-t} - \frac{1}{3} \text{tr} \mathbf{b} \mathbf{F}^{-t}] + K [J - 1] J \mathbf{F}^{-t} \right) + \rho \mathbf{b} & \text{mineral} \\ \text{Div} \left(2\mu \sum_{j=1}^5 \frac{j J^{-\frac{2}{3}j} C_j}{\lambda^{2j-2}} \left[[\mathbf{F}^{-t}]^{j-1} - \frac{1}{3} \mathbf{F}^{-t} (\text{tr} \mathbf{b})^j \right] + \frac{K}{2} [J^2 - 1] \mathbf{F}^{-t} \right) + \rho \mathbf{b} & \text{protein} \end{cases}. \quad (9)$$

4. Modeling failure: a cohesive zone approach

In this contribution, we study failure modes of the bovine enamel. From experimental data [19, 21, 40], it is known that in bovine teeth failure is dominated by fiber debonding or fiber breaking in the vicinity of the protein layers. Thus, it is reasonable to resort to a cohesive zone model as proposed in the early 1960s by Barenblatt [41] and Dugdale [42] to represent the region where a material may separate. Such an approach presupposes the presence of a fracture process zone and, consequently, is computationally less costly - in terms of computational time as well as the complexity of the implementation. The cohesive zone model is widely used in particular for fiber reinforced composites, for fiber breaking and debonding, see e.g. [43, 15, 44, 45].

The key ingredient of a cohesive zone model is the traction-separation relation for the interface. In the cohesive zone, we assume a linear elastic behavior and we account for the evolution of damage. If the traction across the interfaces reaches a critical value, the material sustains damage which is modeled via the damage parameter $d \in [0, 1]$. As the most extreme option ($d = 1$), complete decohesion is achieved. The cohesive zone model is capable of predicting damage evolution, crack initiation and propagation as well as final failure of specimens and structures. Here, we only briefly iterate the main steps.

²The values of the coefficients C_j arise from a series expansion of the inverse Langevin function $\mathcal{L}^{-1}(x)$ with $\mathcal{L}(x) = \coth(x) - 1/x$.

As usual, the material separation is modeled by the displacement jump

$$\llbracket \mathbf{u} \rrbracket = \mathbf{u}^+ - \mathbf{u}^-, \quad (10)$$

where \mathbf{u}^- denotes the displacement field on the left hand side of the crack and \mathbf{u}^+ the counterpart on the right hand side.

The nominal traction stress vector \mathbf{T} consists of three components: T_n, T_s, T_t which are located in a local coordinate system (n denotes the component normal to the interface, s and t are in-plane components). The corresponding components of the separations are $\delta_n, \delta_s, \delta_t$; an effective separation reads

$$\delta_e = \sqrt{\langle \delta_n \rangle^2 + \delta_s^2 + \delta_t^2}. \quad (11)$$

The elastic behavior of the interface is described by a diagonal stiffness matrix, \mathbf{K} , i.e., the elastic traction-separation relations are completely uncoupled:

$$\bar{\mathbf{T}} = \begin{pmatrix} T_n \\ T_s \\ T_t \end{pmatrix} = \begin{bmatrix} K_{nn} & 0 & 0 \\ 0 & K_{ss} & 0 \\ 0 & 0 & K_{tt} \end{bmatrix} \cdot \begin{pmatrix} \delta_n \\ \delta_s \\ \delta_t \end{pmatrix} = \mathbf{K} \cdot \llbracket \mathbf{u} \rrbracket \quad (12)$$

Damage is initiated when the criterion

$$\max \left\{ \frac{\langle T_n \rangle}{T_n^0}, \frac{T_s}{T_s^0}, \frac{T_t}{T_t^0} \right\} = 1, \quad (13)$$

is fulfilled; the evolution equation for the damage parameter d then depends on the effective separation defined in Eq. (11):

$$d = \frac{\delta_e^f (\delta_e^{\max} - \delta_e^i)}{\delta_e^{\max} (\delta_e^f - \delta_e^i)} \quad (14)$$

with δ_e^{\max} being the maximum value of δ_e reached during the loading history, that is, the damage is monotonically increasing. δ_e^i denotes the value of separation at which damage starts, and δ_e^f states the separation at complete decohesion.

In case that damage occurs (i.e., $d \neq 0$), the traction is calculated by

$$\mathbf{T} = [1 - d] \bar{\mathbf{T}} = [1 - d] \mathbf{K} \cdot \llbracket \mathbf{u} \rrbracket. \quad (15)$$

A thermodynamically consistent version of the cohesive zone model, in particular taking into account large rotations and thus derivatives of the normal vector, has been developed in [46]. For the sake of efficiency a simpler version not taking into account finite rotations is used in this contribution, since only single failure modes, either shear or normal separation, occur locally and the cohesive elements will not rotate severely.

The traction is linearly decreasing for increasing separation, when damage is initiated. For decreasing separation after damage initiation, the stress is linearly going to zero with a reduced stiffness, see the dashed line in Fig. 2. It is worth noting that the normal traction is not multiplied by d under compression, i.e.:

$$T_n = \begin{cases} [1 - d]\bar{T}_n, & \text{if } \bar{T}_n \geq 0 \quad (\text{tension}) \\ \bar{T}_n, & \text{if } \bar{T}_n < 0 \quad (\text{compression}) \end{cases} \quad (16)$$

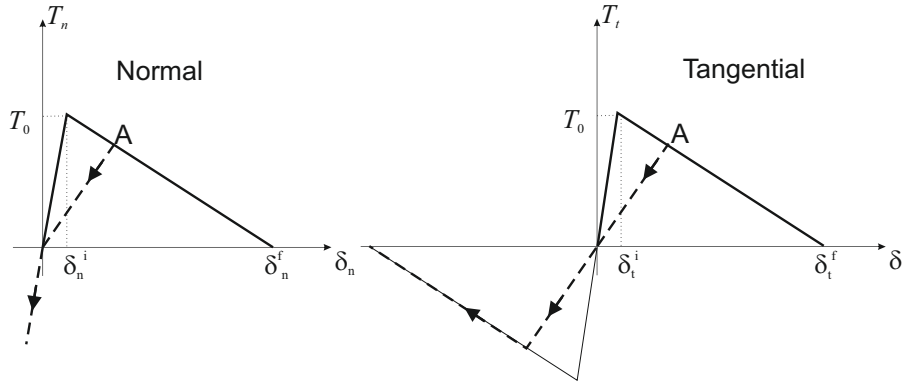


Figure 2: Traction-separation law for uniaxial traction (left: normal; right: tangential) using the damage evolution (14). When the local separation is reversed at point A, the unloading/reverse loading curve is shown by the dashed line.

Remark: Equation (16) does not prevent the displacement jump $[[\mathbf{u}]]$ from becoming negative, i.e., penetration in general is possible, see also the branch for negative traction in Fig. 2. This effect is controlled by the stiffness K_{nn} of the cohesive zone element, i.e., the higher the stiffness the less penetration. In addition, the interface may also have a finite thickness, which at least for a physical interface has its validity. This thickness is then reduced under compression. Throughout this paper, the stiffness of the cohesive element is rather representing a penalty term than a physical parameter. It is set to a value such that $\delta_e^i \approx 10^{-4}\delta_e^f$.

5. Set-up for nanoscale modeling of dental enamel

Enamel is the hardest part of any mammal due to its high volume of very stiff hydroxyapatite fibers. In this work, we study the mechanical properties of the first hierarchical level (level 1), cf. Fig. 1. In this level, the hydroxyapatite (HAP) fibers within the protein matrix are parallel aligned and staggered

together. The mineral volume fraction is about 90%-95% [47]. The diameter of a single HAP fiber is approximately 50 nm, surrounded by a protein layer of a few nanometer thickness, [19]. All simulations are done within the commercial finite element code Abaqus. The entire structure is divided into material with damage-free properties (continuum elements) and interfaces with damage properties (cohesive elements). The cohesive interfaces are a phenomenological representation of various failure mechanisms and do not necessarily coincide with the material's interfaces.

The mechanical behavior of the bovine dental enamel at level 1 is simulated with the help of (i) a representative volume element, RVE, and (ii) a columnar structure. The RVE allows to study the failure mechanisms in detail, while microstructural features, e.g. twisting of the fibers, can only be studied with a model of the complete microstructure. Numerical results for the RVE are shown and discussed in Sect. 5.2 and those for the columnar structure are analyzed in Sect. 5.3.

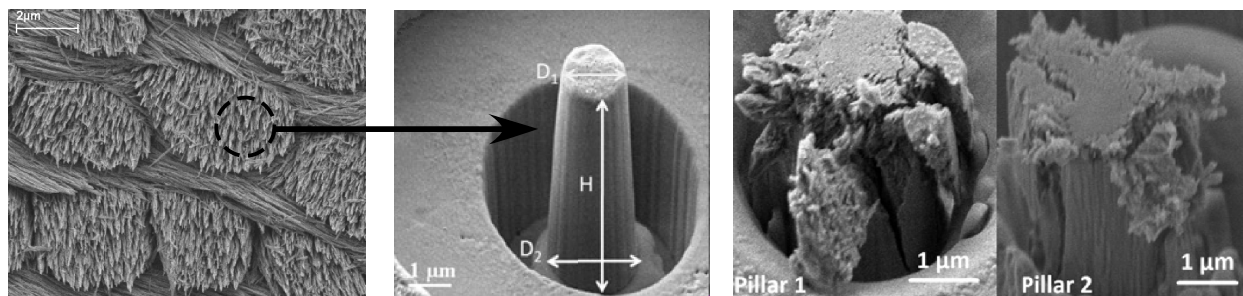


Figure 3: Micropillar compression test of level 1 dental enamel microstructure, picture taken from [40].

The experiments of Bechtle et al. [22, 23] show a uniform parallel and sometimes twisted orientation of the nanofibers inside of bovine enamel³. According to bending tests of Bechtle et al. [22], cracks are likely to propagate along the protein layers. As a consequence, we consider debonding of the fibers at the interfaces as well as breaking of the mineral fibers as possible failure modes in the RVE. Both modes can happen at once. Moreover, it is possible that damage starts and develops at the fiber matrix interface, then stagnates and the mechanism of fiber breaking takes over (or vice versa). Additional micropillar compression tests have been performed by the same group, see [40]. These experiments revealed the main failure mechanisms as fiber buckling, fiber fracture and debonding of fiber bundles from the main column.

There is a diversity in rod shapes and fiber orientation within the rods in the enamel depending on the species, tooth region and angle of the cross-section cut from the tooth [48]. In our opinion, it is reasonable to assume that the bovine rod possesses a honeycomb or circular cross section and is twisted, see e.g., [Fig.

³The paper by An et al. [35] numerically compares a uniform and a non-uniform (gradual change in nanofiber orientation within the rod) fiber arrangement in key-hole shaped rods.

6 (a) and (b) in [23]]. The focus of our work is primarily to learn from biological materials fundamental construction principles which can be applied for the development of synthetic materials.

5.1. Parameter used for modeling the constituents of the dental enamel

The macroscopic mechanical behavior of the tooth strongly depends on the properties of its two components: the mineral HAP fibers and the thin protein matrix layers. For the mineral, experimental data documents a Young's modulus between 80 GPa [49] and 129 GPa [50]. Even though the elasticity is reported to be anisotropic [51, 52], an isotropic averaged Young's modulus of $E = 80$ GPa is used for the longitudinal and transverse orientations. The Poisson ratio in mineral is found to be 0.23 [53]. The uncertainty of these parameters is very large, since it is a biological material, and hence the properties have a large variation even within any tooth, and even more among different mammals. In addition, the fibrils are so small that single aggregates cannot be tested without effect of the boundary or surrounding material.

The literature is even sparser with respect to the damage properties of the constituents. While the strength of HAP-single fibers is known to be in the range of 2 GPa, see [23], the fracture energy, G_m or, alternatively, the fracture toughness, $K_{Ic,m}$, is not reported. In the following, a fracture energy of $G_m = 10 \text{ J/m}^2$ is assumed together with $T_{0,m} = 2$ GPa. From these parameters the critical separation can be calculated as $\delta_{e,m}^f = 10$ nm.

For the protein, an elastic modulus of 900 MPa is reported [23]. We assume a Poisson ratio of 0.495. The fracture strength of the protein also varies in a wide range within 50 to 300 MPa; here we set $T_{0,p} = 200$ MPa with a fracture energy of $G_p = 56 \text{ J/m}^2$, resulting in a critical separation $\delta_{e,p}^f = 1.56 \mu\text{m}$.

The interface between protein and HAP fibers has no deformation but only material separation properties. Since no parameters can be retrieved from experiments due to the very small scale, cohesive model parameters are presumed. The cohesive shear strength is set to $T_{0,deb} = 200$ MPa, the fracture energy to $G_{deb} = 100 \text{ J/m}^2$ ⁴. The resulting critical separation is $\delta_{e,deb}^f = 1.0 \mu\text{m}$.

In summary, we use the following parameters for the simulations: $E_m = 80$ GPa, $\nu_m = 0.23$, $E_p = 900$ MPa and $\nu_p = 0.495$. Consequently, the bulk modulus K and the shear modulus μ_0 are determined via $3K = E/[1 - 2\nu]$ and $2\mu_0 = E/[1 + \nu]$, resulting in $3K_m = 49.38$ GPa, $K_p = 30000$ MPa, $\mu_{0m} = 32.52$ GPa and $\mu_{0p} = 301$ MPa. In case of the protein, the locking stretch λ needs to be specified. Following [37], we set $\lambda = 1$.

⁴The fracture toughness of enamel is approximately $1 \text{ MPa m}^{1/2}$ and the elastic modulus 10GPa. Then, $G_{deb} = K_{Ic,m}^2/E = 100 \text{ J/m}^2$.

5.2. Representative volume element

An equilateral triangular prism is assumed for the shape of the RVE, see Fig. 4 (right). The side length of the RVE's base triangle (see Fig. 5) is always $S = 52$ nm in the simulations. The protein layer between the fibers is 2 nm thick, leading to a hexagon side length of approximately $e_{\text{fib}} = 29$ nm. The length of the mineral fibers is not known. In order to study different failure mechanisms and compound stiffnesses, we vary the fiber aspect ratio $l_{\text{fib}}/e_{\text{fib}} = [1.9, \dots, 20]$. The volume ratio depends slightly on the fiber length, we always obtain a fiber volume fraction of around 90% in the RVE.

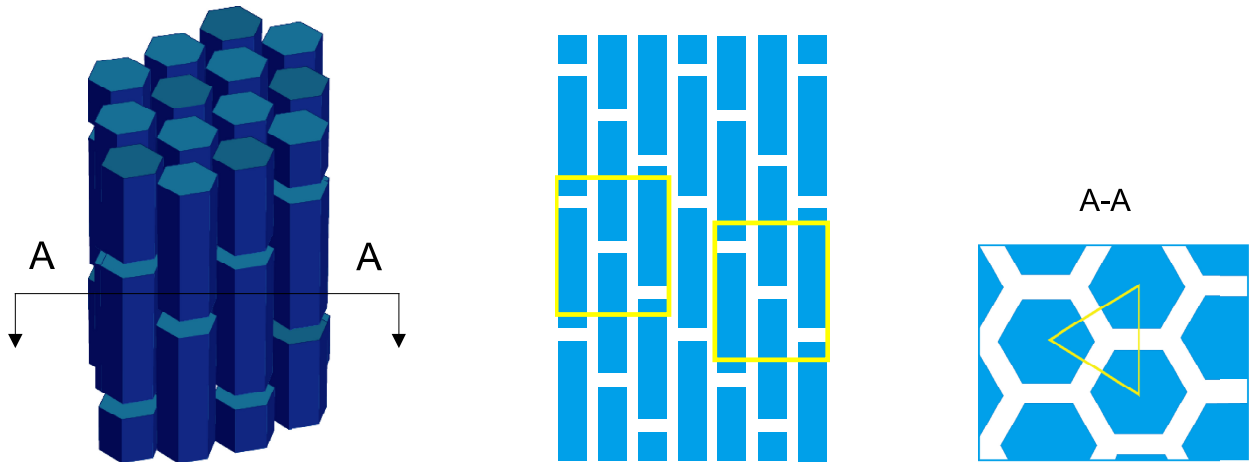


Figure 4: Schematic description of the microstructure of the RVE model. Regular hexagonal prisms are chosen for the fibers. The RVE is a triangular prism indicated by the yellow line.

We assume a perfect RVE, i.e., no pre-cracks and no initial damage. The mesh is built using 3D continuum elements using linear shape functions (8 nodes) and linear cohesive elements (8 nodes). The complete finite element structure is shown in Fig. 5 (left) for the aspect ratio $L/S = 3.8$. The cohesive elements are placed along the side walls of all fibers, and also along the relevant planes normal to the loading direction of the RVE. Fig. 5 (right) shows the cohesive elements.

The applied loading is displacement controlled with a uniaxial displacement in fiber direction (maximum $1 \mu\text{m}$), symmetry conditions for the bottom and the side faces apply. That is, the RVE is exposed to uniaxial straining, which is applied under tension and compression. Tensile deformation leads to failure of the interface and/or fiber breaking, whereas due to the strict boundary conditions of the side faces, failure can hardly occur under compression. However, the compression case is important for the comparison of the stiffness of the structure. As we see in the following, the structure fails before the maximum displacement is reached. All simulations are run using an additional hourglass stiffness in Abaqus. This did not affect the material's response, but improved convergence.

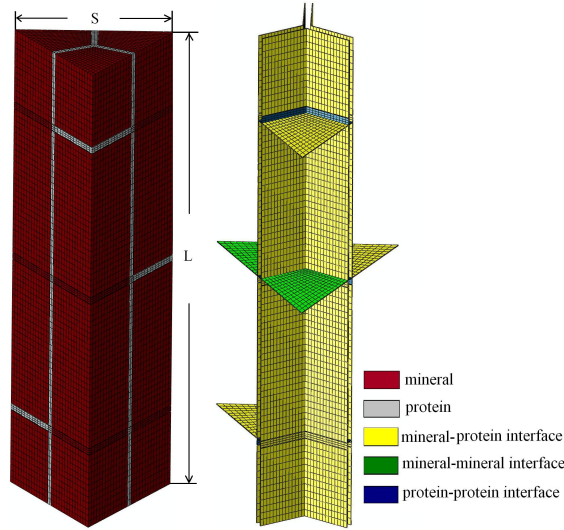


Figure 5: Left: Meshed RVE. The triangular prism has a side length of $S = 52$ nm, the length is shown for the aspect ratio $L/S = 3.8$. Right: Cohesive elements in the model with three different damage properties.

5.3. Columnar structure simulation

The arrangement of the fibers within the rods affects the stiffness and strength of the enamel material. Thus, a columnar microstructure of a number of HAP fibers compounded by protein matrix is modeled. Since the structural dimension of this model is much bigger than the RVE developed in the previous section, some simplifications are introduced. In the current model, the protein matrix is not modeled by continuum elements with the Arruda–Boyce material model, rather cohesive elements are used with elastic properties equivalent to the Young’s and shear moduli given in Sect. 5.1. These cohesive elements are able to model the damage of the fiber matrix interface with the parameters already used in the previous section. It is assumed that the fibers are infinitely long, that is, no debonding at the fiber ends occur. Several parameters (numbers of fibers, twist angle) are varied. The resulting mesh for a fiber diameter of approximately 50 nm (hexagon side length 30 nm) and a protein layer thickness of 5 nm is shown in Fig. 6.

The boundary conditions are such that they reproduce the micro compression test shown in [40], however, with smaller dimensions. The bottom plane is fixed in all directions, the side walls are free surfaces, and the top surface is subject to displacement loading in the direction of the column. Additional simulations are conducted using contact to flat punch (modeled as a rigid surface with and without friction) and with fixed transverse displacement at the top surface, but none of these changes had a significant effect on the results.

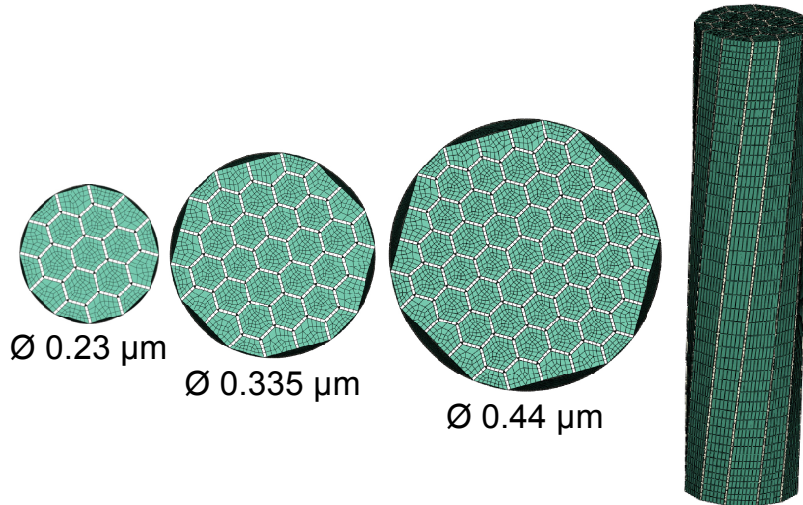


Figure 6: Mesh of the compression column. Different cross section sizes between 0.23 and $0.44 \mu\text{m}$ are studied. The column has a length of $L = 1 \mu\text{m}$ and the regular hexagon of the HAP fiber has a side length of $e_{\text{fib}} = 30 \text{ nm}$. The column twist angle (see right) is varied between 0 and 90° .

6. Numerical results

6.1. Representative volume element

6.1.1. Tension tests

First, numerical tension tests for the nanoscale RVE are performed. We apply a maximum displacement of $1 \mu\text{m}$. The elastic deformations of the standard elements are small. In the cohesive zone elements, however, large deformations may and do occur. Fig. 7 shows the stress-strain response in dependence of the aspect ratio S/L , whereby $S = 52 \text{ nm}$ is kept fixed. We vary the length of the RVE L from 90 nm to 1000 nm . The length dependent behavior is clearly visible. For large aspect ratios ($S/L > 6$), the material withstands high stresses, but damage occurs at smaller strains leading to a small fracture energy, see Fig. 8. In accordance to experimental findings [23], the protein layer is mechanically weaker compared to the mineral fibers.

Further, depending on the aspect ratio S/L , different failure modes occur, cf. in Fig. 9. The change of failure mode leads to a sharp drop in the fracture energy, since much energy is dissipated during debonding along the fiber walls. Both strength and energy are linearly depending on the fiber length due to the stress transfer along the fiber matrix interface as has been reported in [15, 16]. It must be noted that even though the stress drops almost to zero abruptly for the breaking mode, tearing the RVE completely apart happens at very high strains. The soft protein carries the remaining portion of the load further on.

Further comparison with the experimental results of [23] also shows a very good agreement regarding the fracture strength of approximately 1 GPa and the fracture strain of 2% for long nanofibers with aspect ratios of about 300 (aspect ratio $S/L > 6$ in Fig. 7). That is, the first level of the enamel microstructure seems to be designed for high strength, not for high toughness, see Fig. 8. This agrees with [31, 54], where a gradual increase of fracture energy, combined with a decrease in fracture strength from level to level is theoretically predicted, as in level 2 the aspect ratio is much smaller than in level 1. The transition from brittle to damage tolerant behavior is experimentally already measured at aspect ratios of 9 [23], but regarding the uncertainties of the used materials parameters this is in very good agreement with the findings of this simulation were the transition is at an aspect ratio of 6.

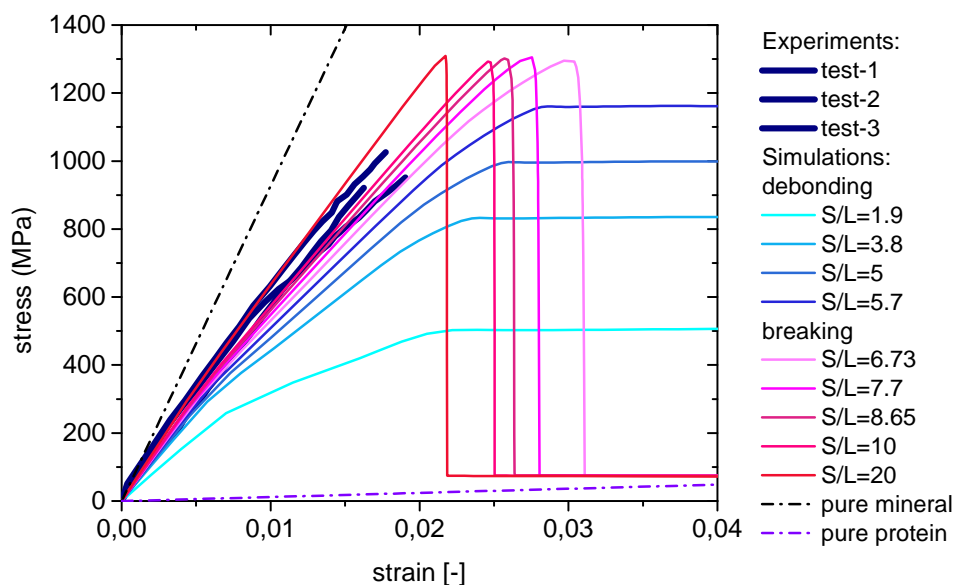


Figure 7: Stress-strain response of the RVE under tension (aspect ratio S/L). Experimental data taken from [23].

Figs. 10-12 depict the material's response for $L = 250$ nm (aspect ratio $S/L = 5$). A discretization of 89884 continuum spatial elements and 12077 cohesive elements is used in these simulations. Damage starts in three protein interfaces and then spreads to the mineral-protein interface. The dental enamel fails due to debonding, as illustrated in Fig. 10. The damage distribution clearly shows a maximum at the protein-mineral interface.

Next, we study a material with $L = 500$ nm (aspect ratio $S/L = 10$). We apply a discretization of 174934 continuum spatial elements and 22661 cohesive elements. The material fails due to breaking, cf. Fig. 13. At the upper interface, the beginning of debonding in longitudinal direction is noticed. Critical separation is first reached in the centered interface (in the protein). This is in accordance to experimental findings

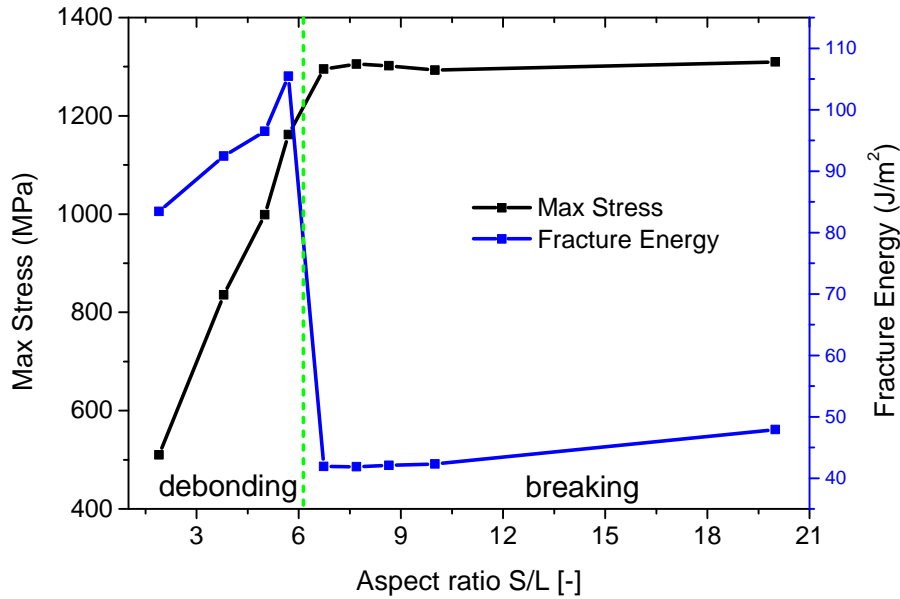


Figure 8: The fracture energy and the maximum stress for the RVE under tensile loading are depicted as a function of the aspect ratio S/L . The longer the rod, the larger the maximum amount of stress the dental enamel can pick up and the less likely the material cracks.

[23] which state that the protein-mineral-interface is the preferential crack path within the dental enamel. As expected, the failing interface plane is the position of the highest stress level (at 2.5% strain), see Fig. 14. Fig. 15 illustrates the stress distribution in the continuum elements at 2.5% strain. As expected, the maximum and minimum stress concentration are found in the vicinity of the mineral interfaces.

6.1.2. Compression tests

The same set-ups as before are simulated under compressive loading. Due to the strong boundary conditions, no failure occurs here, but the elastic behavior is compared with the tensile results. Again, stress vs. strain curves are calculated, they are displayed for two aspect ratios, $L/S = 3.8$ (failure mode under tension: debonding) and $L/S = 10$ (breaking) in Fig. 16. It is clearly visible that the difference between tension and compression is stronger for the debonding case, since damage develops gradually in this case, while sudden unstable fracture occurs in the fiber breaking mode. The difference for $L/S = 10$ has two reasons: On the one hand, some debonding occurs also for high aspect ratios under tension; on the other hand, the material model used for the protein affects the overall strain depending on the loading case.

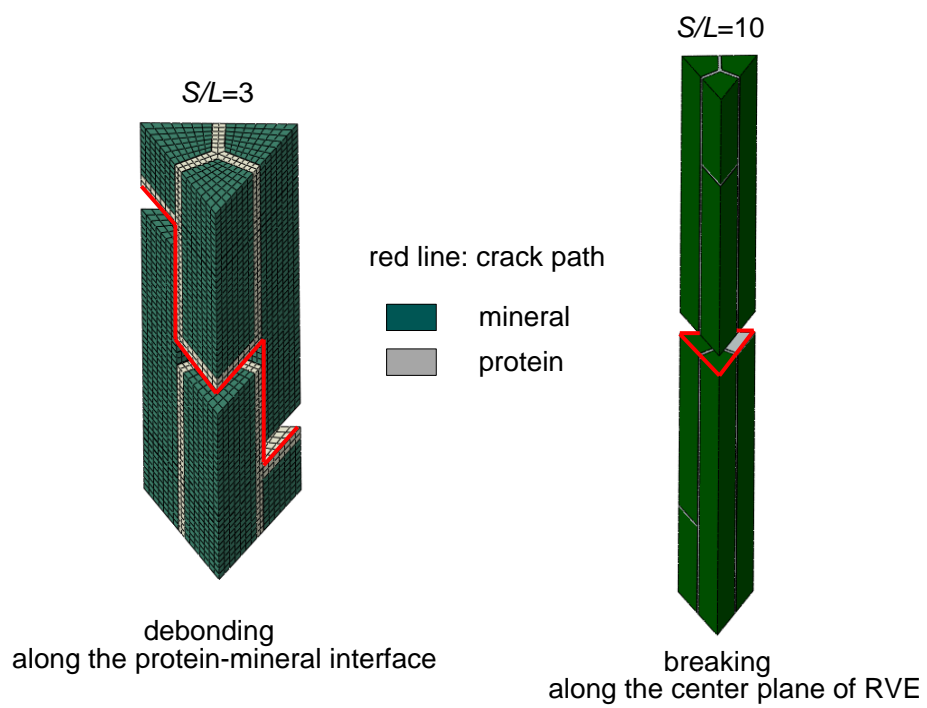


Figure 9: The failure mechanism depends on the aspect ratio S/L . For small values, debonding along the protein-mineral interface occurs. For large values, the material breaks along the center plane of the RVE.

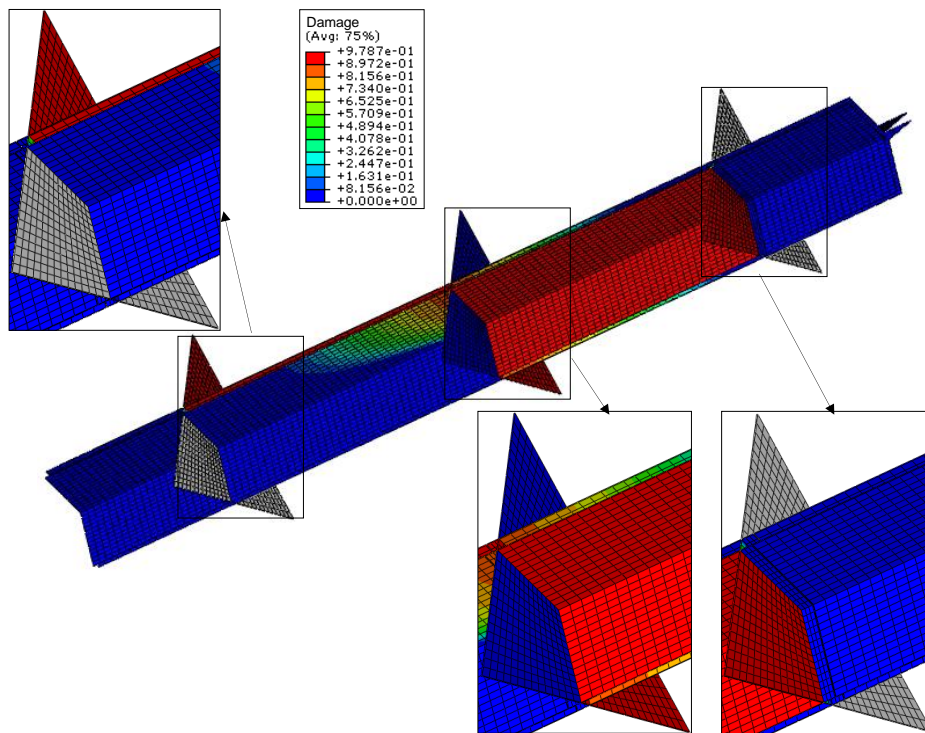


Figure 10: The damage parameter d is plotted for the cohesive elements, $L = 250$ nm (aspect ratio $S/L = 5$, at the end of the simulation). Red corresponds to a fully damaged element, whereas blue indicates a faultless element. Continuum elements are depicted in grey color. Simple tension test.

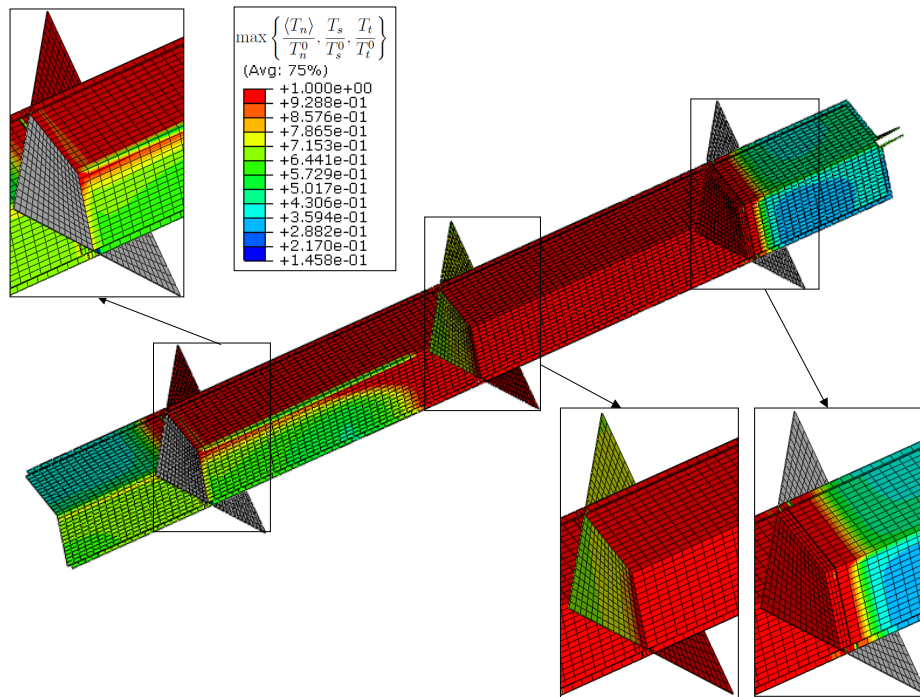


Figure 11: Stress distribution in the cohesive elements, $L = 250$ nm (aspect ratio $S/L = 5$, at maximum stress, approximately 3% strain). Simple tension test.

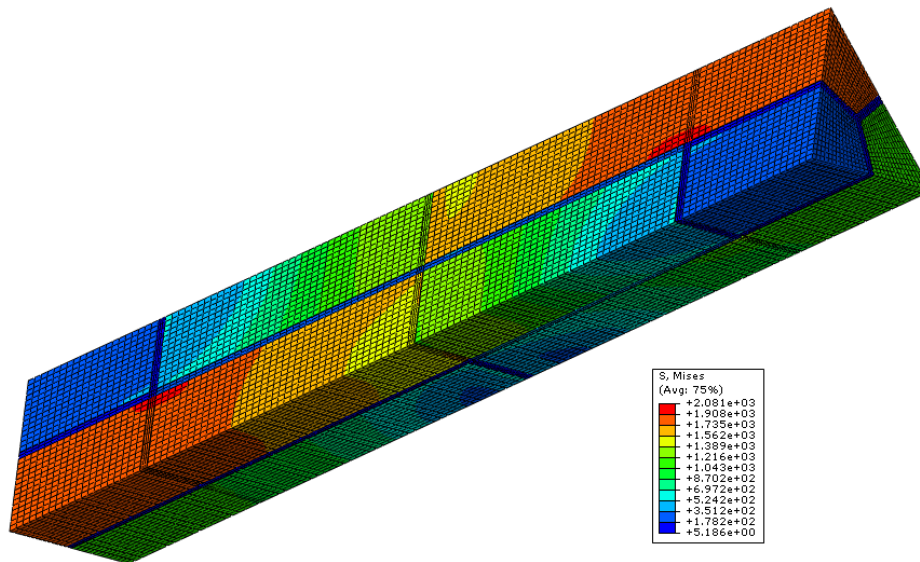


Figure 12: Stress distribution in the continuum elements, $L = 250$ nm (aspect ratio $S/L = 5$, at maximum stress, approximately 3% strain). Simple tension test.

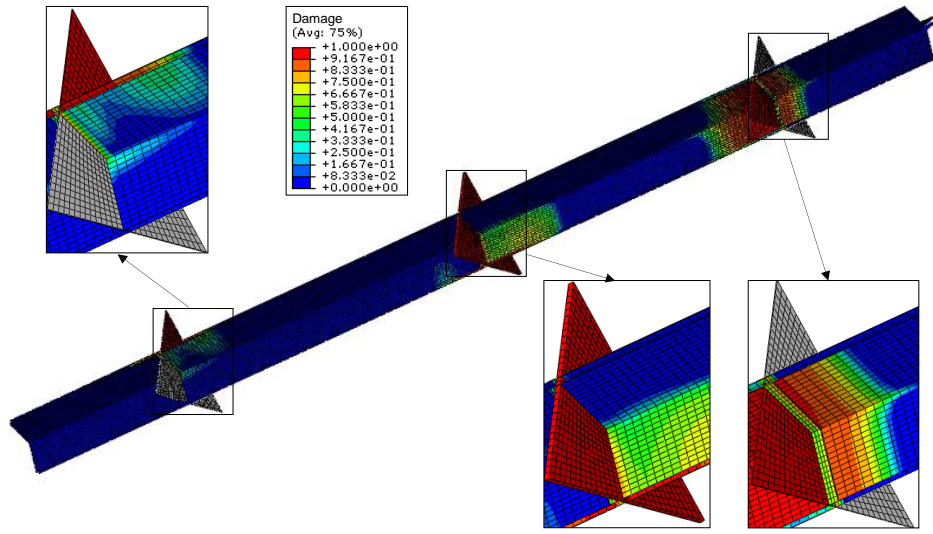


Figure 13: The damage parameter d is plotted for the cohesive elements, $L = 500$ nm (aspect ratio $S/L = 10$, at the end of the simulation). Red corresponds to a fully damaged element, whereas blue indicates a faultless element. Continuum elements are depicted in grey color. Simple tension test.

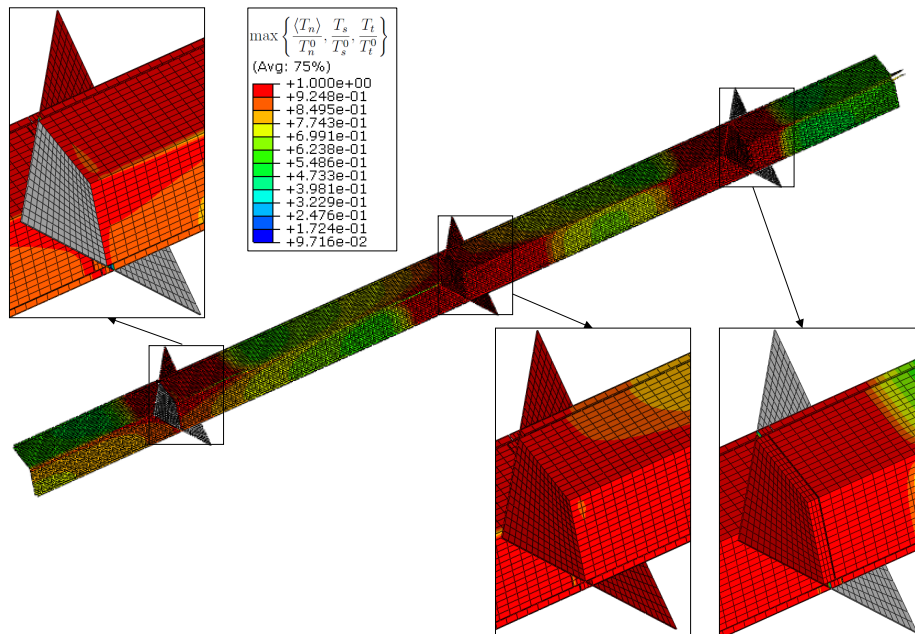


Figure 14: Stress distribution in the cohesive elements, $L = 500$ nm (aspect ratio $S/L = 10$, at maximum stress, approximately 2.5% strain). Simple tension test.

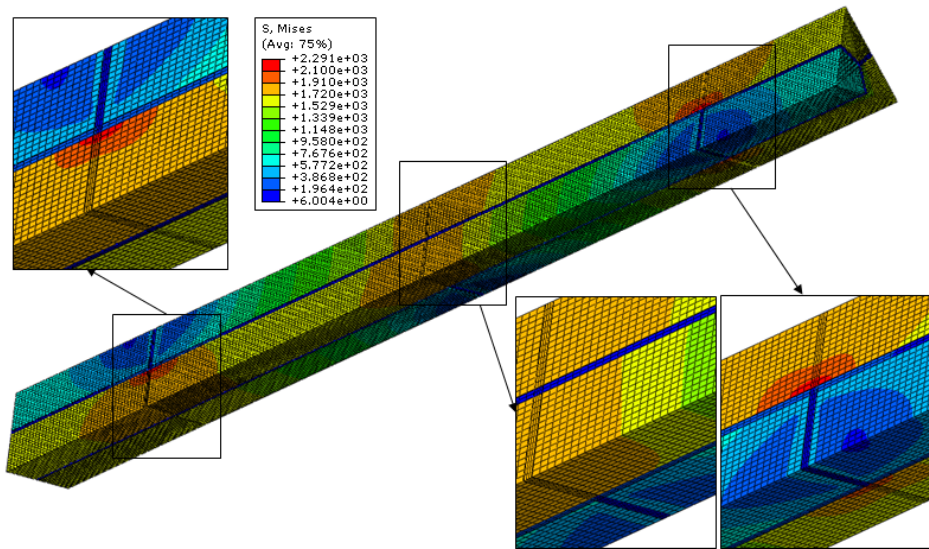


Figure 15: Stress distribution in the continuum elements, $L = 500$ nm (aspect ratio $S/L = 10$, at maximum stress, approximately 2.5% strain). Simple tension test.

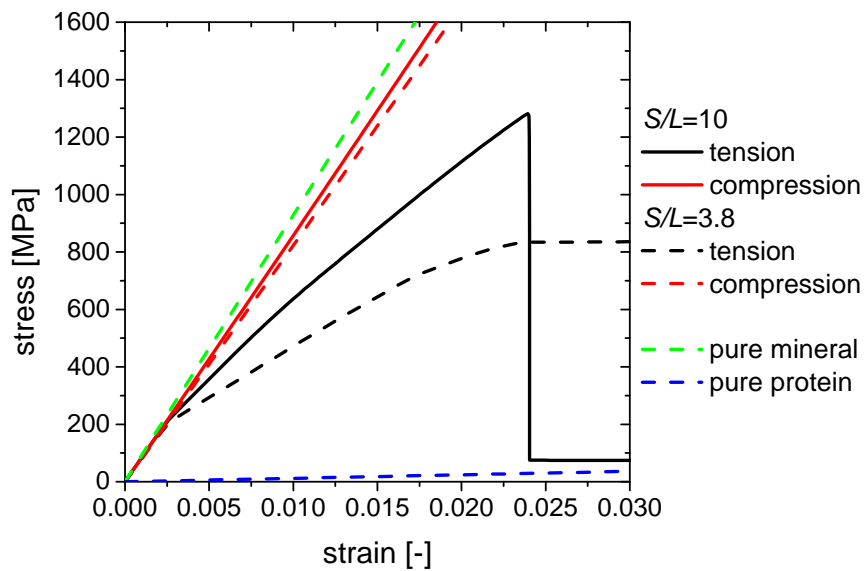


Figure 16: Stress-strain response of the RVE, comparison between tension and compression tests for two selected aspect ratios S/L .

6.2. Columnar structure simulation

The finite element simulations of the column microstructure are performed with the three different cross sections as shown in Fig. 6 and for twist angles between 0 and 90°. In each simulation, the elastic stiffness in terms of stress divided by strain, calculated at 0.4% strain, is calculated. The result serves as the average Young's modulus of the enamel in the fiber direction. Since the fibers are infinitely long, the 0° twist simulation leads to the same stiffness as the theoretical Voigt bound, approximately 68 GPa. The stiffness decreases significantly with the twist angle, and also with the size of the column (different sizes are calculated for a twist angle of 45°). This effect is due to the plane of the protein layer, which is vertical in the untwisted case, turning into a more and more inclined position. This is obvious when the angle increases, see Fig. 17a; but holds also for an increasing radius, see Fig. 17b, since the path length increases for the outermost fibers, and so does the inclination angle. The size dependence in Fig. 17 shows that there is hardly any difference between tension and compression; this is expected as long as no buckling occurs.

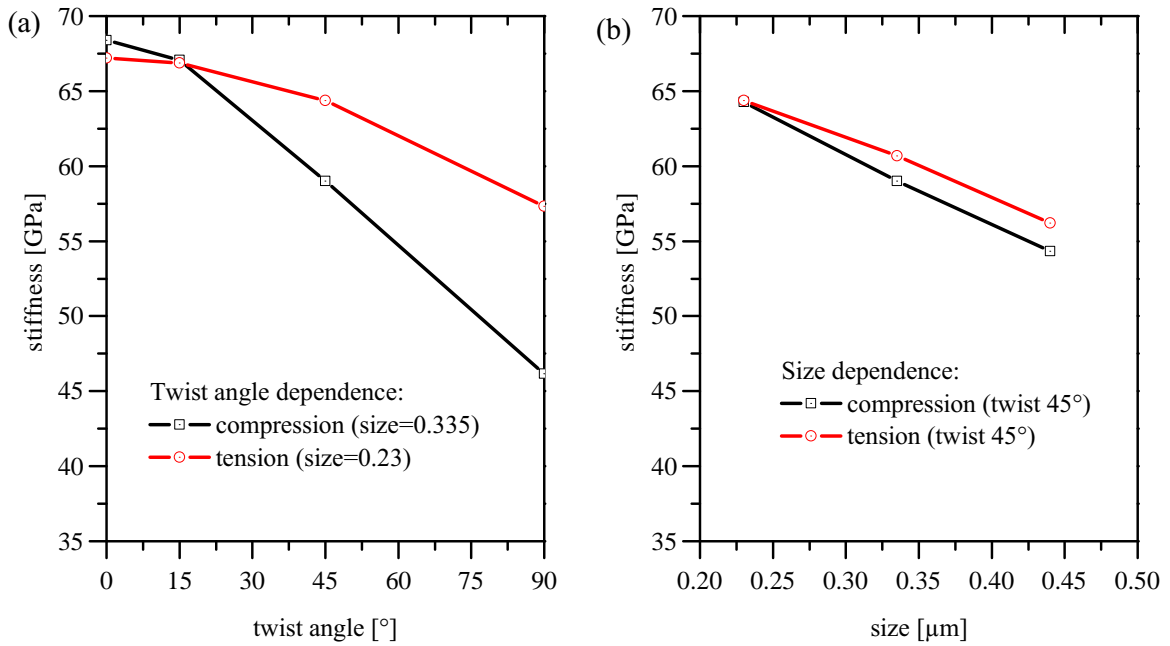


Figure 17: Effect of (a) twist angle and (b) column diameter on the stiffness of the column under tension and compression.

The experiments conducted by Yilmaz et al. [40] show that significant damage starts between 2% and 3% strain. In the simulations a maximum compressive displacement of 0.1 mm (=10% strain) is applied. The results indicate that the structure can withstand very high loads without damage, if the fibers are not twisted in the model. However, a slight twist (15%) is sufficient to produce damage and fracture the specimen. The stress-strain behavior of several sizes and twist angles are shown in Fig. 18. The simulation usually aborts

before the maximum displacement was reached, but at the end of the simulation damage evolves heavily from the outmost cohesive protein layers towards the center of the column, such that the load is decreasing. One can see that the strength of the column (highest stress) depends on both the size and the twist angle. In [40], the columns often break at their heads. This cannot be reproduced in the simulations, since small imperfections at the column head coming from the FIB production and the exact contact conditions are difficult to model.

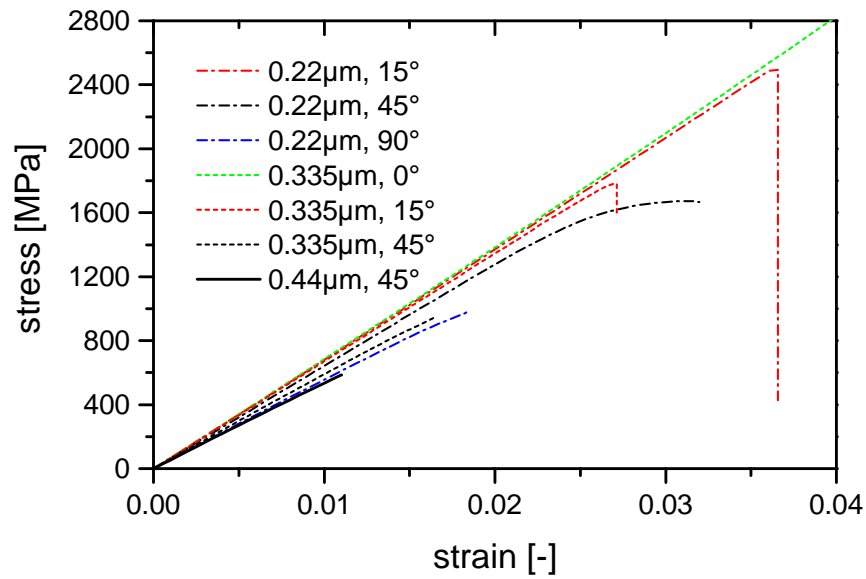


Figure 18: Columnar structure, compression test: Stress-strain curves.

7. Summary

The goal of our work is to understand the structure and property relationship of hierarchically structured biological materials, which could contribute biomimetic material research using the biological systems as models for engineering applications. A bovine tooth consists of different layers, of which dental enamel is the outermost one. The dental enamel is a hierarchical composite which consists of two natural materials, e.g., mineral and protein.

We presented a model of the mechanical behavior of bovine dental enamel, with emphasis on the failure behavior. The microstructure of bovine teeth is very similar to that of human teeth [55, 56]. Due to their size and the larger availability, many experiments are performed for bovine rather than human teeth. The model has been validated against experimental data and we achieved a good agreement. The proposed model captures accurately size effects and the dependence of the failure mode in regard to the aspect ratio of fibers. Various failure mechanisms are represented phenomenologically by cohesive interfaces.

The numerical realization relies on the idea of a complete scale separation. The simulations study the first hierarchy level of the bovine teeth. We consider a three-dimensional, triangular prism representative volume element.

Findings:

- Long fibers definitely fail by breaking, but some amount of debonding occurs in any case.
- Damage under compression needs some imperfection. This might be a defect, or a twist, maybe also an ending fiber, which then impinges and damages the protein matrix. A long slim column can also fail under buckling.
- The twist angle reduces the strength of the column significantly, that is, for large columns containing many more fibers than simulated here, a small angle will suffice to decrease the strength to the values observed in the experiment.

The optimized mechanical functioning of these biological materials, like being hard and damage tolerant at the same time is a desirable property for engineering applications. Thus, there are considerable efforts underway to understand how these mechanical properties are governed through a hierarchical combination of the hard and soft structural components. In this view, the modeling of dental enamel was undertaken in this study. And one of the finding was that the optimization of fracture energy and fracture strength can be regulated by the hard particle aspect ratio. For example, this could serve as design parameter for bio-inspired artificial fiber-reinforced composite materials.

Further, based on the developed model, it is now possible to adjust material parameters and geometrical features for the first level of hierarchy which are difficult to determine experimentally, such as the twist angle, by fitting the experimentally measured strength and stiffness from micro bending and micro compression tests. From the existing literature it is well known that strength and stiffness are reduced by adding further levels of hierarchy simply due to the fact that the percentage of soft phase is continuously increasing with each level. The numerical results on the effects of the twist angle and the column diameter under tension and compression on the material's stiffness give rise towards an optimized design of a hierarchical advanced ceramics. It is, however, unclear if and how further levels of hierarchy may be beneficial with regard to other properties, such as the fracture toughness. Once this question is answered, the resulting model is applicable studying combinations of materials and geometries for various materials and hierarchy designs. Based on such an approach it will be possible to clarify if and how the different levels of hierarchy should be tailored to obtain a synthetic hierarchical material with improved macroscopic properties.

8. Acknowledgements

The authors gratefully acknowledge stimulating discussions with Erica T. Lilleodden (Helmholtz institute) on the structural properties of the different hierarchical levels in bovine teeth. This work was funded by DFG through SFB 986 "Tailor-Made Multi-Scale Materials Systems - M³". The authors would like to thank the anonymous reviewers for their helpful and constructive comments that greatly contributed to improving the manuscript.

9. References

- [1] P.-Y. Chen, A.-M. Lin, A. Stokes, Y. Seki, S. Bodde, J. McKittrick, M. Meyers, Structural biological materials: overview of current research, *JOM* 60 (6) (2008) 23–32.
- [2] P. Fratzl, R. Weinkamer, Nature's hierarchical materials, *Progress in Materials Science* 52 (8) (2007) 1263–1334.
- [3] M. A. Meyers, P.-Y. Chen, A. Y.-M. Lin, Y. Seki, Biological materials: structure and mechanical properties, *Progress in Materials Science* 53 (1) (2008) 1–206.
- [4] I. Aksay, M. Trau, S. Manne, I. Honma, N. Yao, L. Zhou, P. Fenter, P. Eisenberger, S. Gruner, et al., Biomimetic pathways for assembling inorganic thin films, *Science* (1996) 892–897.
- [5] P. Podsiadlo, A. Kaushik, E. Arruda, A. Waas, B. Shim, J. Xu, H. Nandivada, B. Pumplun, J. Lahann, A. Ramamoorthy, et al., Ultrastrong and stiff layered polymer nanocomposites, *Science* 318 (5847) (2007) 80–83.
- [6] A. Sellinger, P. Weiss, A. Nguyen, Y. Lu, R. Assink, W. Gong, C. Brinker, Continuous self-assembly of organic–inorganic nanocomposite coatings that mimic nacre, *Nature* 394 (6690) (1998) 256–260.
- [7] Z. Tang, N. A. Kotov, S. Magonov, B. Ozturk, Nanostructured artificial nacre, *Nature materials* 2 (6) (2003) 413–418.
- [8] S. Deville, E. Saiz, R. K. Nalla, A. P. Tomsia, Freezing as a path to build complex composites, *Science* 311 (5760) (2006) 515–518.

- [9] E. Munch, D. Launey, M. Alsem, E. Saiz, A. Tomsia, R. Ritchie, Tough, bio-inspired hybrid materials, *Science* 322 (5907) (2008) 1516–1520.
- [10] K. Brandt, V. Salikov, H. Özcoban, P. Staron, A. Schreyer, L. Prado, K. Schulte, S. Heinrich, G. Schneider, Novel ceramic–polymer composites synthesized by compaction of polymer-encapsulated tio₂-nanoparticles, *Composites Sci. Tech.* 72 (1) (2011) 65–71.
- [11] L. Wang, J. Song, C. Ortiz, M. Boyce, Anisotropic design of a multilayered biological exoskeleton, *J. Mater. Res.* 24 (12).
- [12] L. Wang, J. Song, C. Ortiz, M. Boyce, Enamel-a metallic-like deformable biocomposite, *Journal of Dentistry* 35 (2007) 431–427.
- [13] S. Ghosh, K. Lee, P. Raghavan, A multi-level computational model for multi-scale damage analysis in composite and porous materials, *Int. J. Solids Struct.* 38 (2001) 2335–2385.
- [14] I. M. Gitman, H. Askes, L. J. Sluys, Representative volume: Existence and size determination, *Engineering Fracture Mechanics* 74 (2007) 2518–2534.
- [15] I. Scheider, Y. Chen, A. Hinz, N. Huber, J. Mosler, Size effects in short fibre reinforced composites, *Engineering Fracture Mechanics* 100 (2013) 17–27. doi:10.1016/j.engfracmech.2012.05.005.
URL <http://www.sciencedirect.com/science/article/pii/S0013794412002007>
- [16] I. Scheider, T. Xiao, N. Huber, J. Mosler, On the interaction between different size effects in fibre reinforced pmma: towards composites with optimised fracture behaviour, *Comp. Mat. Sci.* accepted. doi:submitted.
- [17] C. Bodecker, Enamel lamellae and their origin, *J. Dent. Res.* 32 (1953) 239–245.
- [18] H. Chai, J. Lee, P. Conatantino, P. Lucas, B. Lawn, Remarkable resilience of teeth, *PNAS Early Edition* 106 (2009) 1–5.
- [19] S. Ang, A. Schulz, R. Pacher Fernandes, G. Schneider, Sub-10-micrometer toughening and crack tip toughness of dental enamel, *J. Mech. Behavior Biomedical Mat.* 4 (2011) 423–432.
- [20] D. Bajaj, D. Arola, On the r-curve behavior of human tooth enamel, *Biomaterials* 30 (2009) 4037 – 4046.
- [21] S. Bechtle, T. Fett, G. Rizzi, S. Habelitz, G. Schneider, Mixed-mode stress intensity factors for kink cracks with finite kink length loaded in tension and bending: Application to dentin and enamel, *J. Mech. Behavior Biomedical Mat.* 3 (4) (2010) 303 – 312.
- [22] S. Bechtle, S. Habelitz, A. Klocke, T. Fett, G. Schneider, The fracture behaviour of dental enamel, *Biomaterials* 31 (2) (2010) 375 – 384.
- [23] S. Bechtle, H. Özcoban, E. Lilleodden, N. Huber, A. Schreyer, M. Swain, G. Schneider, Hierarchical flexural strength of enamel: transition from brittle to damage-tolerant behaviour, *Journal of the Royal Society Interface* doi: 10.1098/rsif.2011.0498.
- [24] S. Bechtle, H. Özcoban, E. Yilmaz, T. Fett, G. Rizzi, E. Lilleodden, N. Huber, A. Schreyer, M. Swain, G. Schneider, A method to determine site-specific, anisotropic fracture toughness in biological materials, *Scr. Mat.* 66 (8) (2012) 515 – 518. doi:10.1016/j.scriptamat.2011.12.027.
URL <http://www.sciencedirect.com/science/article/pii/S1359646211007755>
- [25] V. Dusevich, C. Xu, Y. Wang, M. Walker, J. Gorski, Identification of a protein-containing enamel matrix layer which bridges with the dentine-enamel junction of adult human teeth, *Arch. Oral Bio.* 57 (2012) 1585–1594.
- [26] G. Anstis, P. Chantikul, B. Lawn, D. Marshall, A critical evaluation of indentation techniques for measuring fracture toughness: I, direct crack measurements, *J Am Ceram Soc* 64 (1981) 533–538.
- [27] R. Hassan, A. Caputo, R. Bunshah, Fracture toughness of human enamel, *J Dent* 60 (1981) 820–827.
- [28] S. Park, J. Quinn, E. Romberg, D. Arola, On the brittleness of enamel and selected dental materials, *Dent Mater* 24 (2008) 1477–1485.
- [29] R. Nalla, J. Kruzic, R. Ritchie, On the origin of the toughness of mineralized tissue: microcracking or crack-bridging, *Bone* 34 (2004) 790–798.

- [30] V. Imbeni, J. Kruzic, G. Marshall, S. Marshall, R. Ritchie, The dentin-enamel junction and the fracture of human teeth, *Nature materials* 4 (2005) 229–232.
- [31] H. Gao, Application of fracture mechanics concepts to hierarchical biomechanics of bone and bone-like materials, *Int. J. Fract.* 138 (2006) 101–137.
- [32] I. Ichim, Q. Li, W. Li, M. Swain, J. Kieser, Modelling of fracture behaviour in biomaterials, *Biomaterials* 28 (7) (2007) 1317 – 1326.
- [33] A. Barani, A. Keown, M. Bush, J.-W. Lee, H. Chai, B. Lawn, Mechanics of longitudinal cracks in tooth enamel, *Acta Biomaterialia* 7 (5) (2011) 2285 – 2292.
- [34] B. An, R. Wang, D. Arola, D. Zhang, The role of property gradients on the mechanical behavior of human enamel, *J. Mech. Behavior Biomedical Mat.* 9 (2012) 63 – 72.
- [35] B. An, R. Wang, D. Zhang, Role of crystal arrangement on the mechanical performance of enamel, *Acta Biomaterialia* 8 (10) (2012) 3784 – 3793.
- [36] H. Yao, H. Gao, Multi-scale cohesive laws in hierarchical materials, *Int. J. Solids Structures* 44 (25–26) (2007) 8177 – 8193.
- [37] X. Wu, M. E. Levenston, E. L. Chaikof, A constitutive model for protein-based materials, *Biomaterials* 27 (30) (2006) 5315 – 5325. doi:10.1016/j.biomaterials.2006.06.003.
URL <http://www.sciencedirect.com/science/article/pii/S0142961206005291>
- [38] E. Arruda, M. Boyce, A three-dimensional constitutive model for the large stretch behavior of rubber elastic materials, *J. Mech. Phys. Solids* 41 (2) (1993) 389 – 412. doi:10.1016/0022-5096(93)90013-6.
URL <http://www.sciencedirect.com/science/article/pii/0022509693900136>
- [39] L. Han, L. Wang, J. Song, M. Boyce, C. Ortiz, Direct quantification of the mechanical anisotropy and fracture of an individual exoskeleton layer via uniaxial compression of micropillars, *Nano Letters* 11 (9) (2011) 3868–3874.
- [40] E. Yilmaz, S. Bechtle, H. Özcoban, A. Schreyer, G. Schneider, Fracture behavior of hydroxapatite nanofibers in dental enamel under micropillar compression, *Scripta Materialia* doi: 10.1016/j.scriptamat.2012.11.007.
- [41] G. Barenblatt, The mathematical theory of equilibrium cracks in brittle fracture, *Adv. Appl. Mech.* 7 (1962) 55–129.
- [42] D. Dugdale, Yielding of steel sheets containing slits, *J Mech Phys Solids* 8 (1960) 100–108.
- [43] N. Chandra, H. Li, C. Shet, H. Ghonem, Some issues in the application of cohesive zone models for metal-ceramic interface, *Int. J. Solids Struct.* 39 (2002) 2827–2855.
- [44] V. Tvergaard, Model studies of fibre breakage and debonding in a metal reinforced by short fibres, *J Mech Phys Solids* 41 (1993) 1309–1326.
- [45] H. Wang, H. Zhou, L. Mishnaevsky Jr., P. Brondstedt, L. Wang, Single fibre and multifibre unit cell analysis of strength and cracking of unidirectional composites, *Comput. Mater. Sci* 46 (2009) 810–820.
- [46] J. Mosler, I. Scheider, A thermodynamically and variationally consistent class of damage-type cohesive models, *J Mech Phys Solids* 59 (2011) 1647–1668. doi:10.1016/j.jmps.2011.04.012.
URL <http://www.sciencedirect.com/science/article/pii/S0022509611000743>
- [47] Z. Xie, M. Swain, P. Munroe, M. Hoffman, On the critical parameters that regulate the deformation behaviour of tooth enamel, *Biomaterials* 29 (17) (2008) 2697 – 2703.
- [48] C. Wang, Y. Li, X. Wang, L. Zhang, B. Fu, The enamel microstructures of bovine mandibular incisors, *Anatomical Record: Adv. Integrative Anatomy Evolutionary Bio.* 295 (10) (2012) 1698–1706.
- [49] M. Akao, H. Aoki, K. Kato, Mechanical properties of sintered hydroxyapatite for prosthetic applications, *J. Mat. Sci.* 16 (1981) 809–812. doi:10.1007/BF02402799.
URL <http://dx.doi.org/10.1007/BF02402799>
- [50] S. Ang, E. Bortel, M. Swain, A. Klocke, G. Schneider, Size-dependent elastic/inelastic behavior of enamel over millimeter

and nanometer length scales, *Biomaterials* 31 (2010) 1955 – 1963.

- [51] B. Bar-On, H. D. Wagner, Enamel and dentin as multi-scale bio-composites, *J. Mech. Behavior Biomedical Mat.* 12 (2012) 174–183.
- [52] H. Xu, D. Smith, S. Jahanmir, E. Romberg, J. Kelly, V. Thompson, E. Rekow, Indentation damage and mechanical properties of human enamel and dentin, *Journal of Dental Research* 77 (3) (1998) 472–480.
- [53] N. Waters, Some mechanical and physical properties of teeth, In: Vincent, J.F.V., Currey, J.D. (Eds.), *The Mechanical Properties of Biological Materials*. Cambridge University Press, Cambridge (1980) 99–136.
- [54] M. Meyers, P. Chen, M. Lopez, Y. Seki, A. Lin, Biological materials: A materials science approach, *J Mech Behavior Biomedical Mat* 4 (2011) 626–657.
- [55] L. Oesterle, W. Shellhart, G. Belanger, The use of bovine enamel in bonding studies, *Am. J. Ortho.* 114 (1998) 514–520.
- [56] R. Sanches, C. Otani, A. Damiao, W. Miyakawa, Afm characterization of bovine enamel and dentine after acid etching, *Micron* 40 (2009) 502–506.